

Hints of spin-orbit resonances in the binary black hole population

Vijay Varma,^{1,2,3,*} Sylvia Biscoveanu,^{4,5} Maximiliano Isi,^{4,5,†} Will M. Farr,^{6,7} and Salvatore Vitale^{4,5}

¹*Department of Physics, Cornell University, Ithaca, New York 14853, USA*

²*Cornell Center for Astrophysics and Planetary Science, Cornell University, Ithaca, New York 14853, USA*

³*Max Planck Institute for Gravitational Physics (Albert Einstein Institute), Am Mühlenberg 1, Potsdam 14476, Germany*

⁴*LIGO Laboratory, Massachusetts Institute of Technology, Cambridge, Massachusetts 02139, USA*

⁵*Department of Physics and Kavli Institute for Astrophysics and Space Research, Massachusetts Institute of Technology, 77 Massachusetts Ave, Cambridge, MA 02139, USA*

⁶*Department of Physics and Astronomy, Stony Brook University, Stony Brook NY 11794, USA*

⁷*Center for Computational Astrophysics, Flatiron Institute, New York NY 10010, USA*

(Dated: January 20, 2022)

Binary black hole spin measurements from gravitational wave observations can reveal the binary’s evolutionary history. In particular, the spin orientations of the component black holes within the orbital plane, ϕ_1 and ϕ_2 , can be used to identify binaries caught in the so-called spin-orbit resonances. In a companion paper, we demonstrate that ϕ_1 and ϕ_2 are best measured near the merger of the two black holes. In this work, we use these spin measurements to provide the first constraints on the full six-dimensional spin distribution of merging binary black holes. In particular, we find that there is a preference for $\Delta\phi = \phi_1 - \phi_2 \sim \pm\pi$ in the population, which can be a signature of spin-orbit resonances. We also find a preference for $\phi_1 \sim -\pi/4$ with respect to the line of separation near merger, which has not been predicted for any astrophysical formation channel. However, the strength of these preferences depends on our prior choices, and we are unable to constrain the widths of the ϕ_1 and $\Delta\phi$ distributions. Therefore, more observations are necessary to confirm the features we find. Finally, we derive constraints on the distribution of recoil kicks in the population, and use this to estimate the fraction of merger remnants retained by globular and nuclear star clusters. We make our spin and kick population constraints publicly available.

Introduction.— Binaries of spinning black holes (BHs) serve as a unique astrophysical laboratory for a range of relativistic phenomena. For example, if the BH spins χ_1 and χ_2 are aligned with the orbital angular momentum \mathbf{L} , the orientations of the orbital plane and the spins remain fixed during the inspiral (cf. Fig. 1 for definitions of the binary BH spin parameters). However, if the spins are tilted with respect to \mathbf{L} , relativistic spin-orbit and spin-spin coupling cause the orbital plane and the spins to precess [1, 2].

While the tilt angles θ_1 and θ_2 control precession, the orbital-plane spin angles ϕ_1 and ϕ_2 play a central role in binaries undergoing spin-orbit resonances (SORs) [3]. For these binaries, the χ_1 , χ_2 and \mathbf{L} vectors become locked into a common resonant-plane such that $\Delta\phi = \phi_1 - \phi_2$ is fixed at 0 or $\pm\pi$ as the binary precesses. Refs. [4, 5] pointed out that this locking is a limiting case of librating states near $\Delta\phi \sim 0$ or $\pm\pi$. For simplicity, we will follow previous literature [6–8] and refer to the more general librating states as SORs. While evidence for precession has been found in the astrophysical binary BH population [9], SORs have not yet been observed even though they are expected in some astrophysical scenarios. For example, stellar binaries can cluster near these resonances if supernova natal kicks and stellar tides are significant [10, 11].

Another important relativistic effect that gets amplified for spinning binaries is the gravitational recoil. Gravitational waves (GWs) can carry away linear momentum

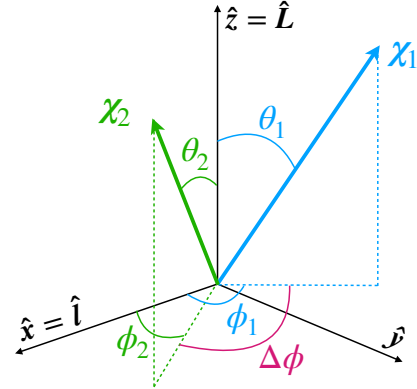


Figure 1. The BH spins are represented by 3-vectors χ_1 and χ_2 , with index 1 (2) denoting the heavier (lighter) BH. We parameterize the spins by their dimensionless magnitudes $\chi_1, \chi_2 \leq 1$, tilts θ_1, θ_2 w.r.t the orbital angular momentum \mathbf{L} [12], and orbital-plane spin angles ϕ_1, ϕ_2 w.r.t the line of separation \mathbf{l} from the lighter to the heavier BH. Finally, $\Delta\phi = \phi_1 - \phi_2$.

from the binary, imparting a recoil or kick velocity to the merger remnant [13–16]. These velocities can reach values up to ~ 5000 km/s for precessing binaries [17–19], large enough to be ejected from any host galaxy [20]. Kick measurements from GW observations [21] can be used to constrain the formation of heavy BHs via successive mergers [22]. However, the kick depends very sensitively on the orbital-plane spin angles [23].

GW observations by LIGO [24] and Virgo [25] have en-

* vijay.varma@aei.mpg.de; Klarman fellow; Marie Curie fellow

† NHFP Einstein fellow

abled increasingly precise constraints on the astrophysical distributions of BH spin magnitudes and tilts [9, 26], but the distributions of the orbital-plane spin angles remain unconstrained. Constraining these distributions would allow us to understand the prevalence of SORs and merger kicks in nature. The biggest obstacle for this, however, is the difficulty in measuring ϕ_1 , ϕ_2 and $\Delta\phi$ from individual GW events with current detectors [6–8, 27–29].

However, in a companion paper, Varma *et al.* [30], we show that this can be greatly improved by measuring the spins near the merger, in particular, at a fixed *dimensionless* reference time $t_{\text{ref}}/M = -100$ before the peak of the GW amplitude, rather than the traditional choice of a fixed GW frequency of $f_{\text{ref}} = 20$ Hz. Here $M = m_1 + m_2$ is the total (redshifted) mass of the binary with component masses $m_1 \geq m_2$, and we set $G = c = 1$. Ref. [30] shows that this improvement can be attributed to the waveform being more sensitive to variations in the orbital-plane spin angles near the merger. In particular, measuring the spins near the merger leads to improved constraints for ϕ_1 and ϕ_2 for several events in the latest GWTC-2 catalog [31–35] released by the LIGO-Virgo Collaboration. While the $\Delta\phi$ measurements are not significantly impacted, Ref. [30] shows that this parameter will also be better constrained with louder signals expected in the future.

In this *Letter*, we use the spin constraints from Ref. [30] to perform the first measurement of the full spin distribution in the astrophysical binary BH population. In particular, we identify a preference for $\Delta\phi \sim \pm\pi$, which can be a signature of SORs. Next, given the spin population, we derive constraints on the kick population. Finally, we use the kick constraints to estimate the fraction of merger remnants retained by globular and nuclear star clusters.

Methodology.— The first step in our analysis is to estimate the binary BH parameters from individual GW signals, which is done following Bayes’ theorem [36]:

$$p(\Theta|d) \propto \mathcal{L}(d|\Theta) \pi(\Theta), \quad (1)$$

where $p(\Theta|d)$ is the *posterior* probability distribution of the binary parameters Θ given the observed data d , $\mathcal{L}(d|\Theta)$ is the *likelihood* of the data given Θ , and $\pi(\Theta)$ is the *prior* probability distribution for Θ . The full set of binary parameters Θ is 15 dimensional [31], and includes the masses and spins of the component BHs as well as extrinsic properties such as the distance and sky location.

In this work, we use the posteriors samples from Ref. [30], obtained using the numerical relativity (NR) surrogate waveform model NRSur7dq4 [37], with the spins measured at $t_{\text{ref}}/M = -100$. NRSur7dq4 accurately reproduces precessing NR simulations and is necessary to reliably measure the orbital-plane spin angles [30]. GWTC-2 includes a total of 46 binary BH events. However, because NRSur7dq4 only encompasses ~ 20 orbits before merger, it can only be applied to the shorter signals with $M \gtrsim 60 M_\odot$ [37]. This reduces our set of events to 31;

these events are listed in Tab. I of Ref. [30].

Given the posterior samples $p(\Theta|d)$ for the individual events, we want to measure the astrophysical distribution of the full spin degrees of freedom, $\mathbb{S} = \{\chi_1, \chi_2, \theta_1, \theta_2, \phi_1, \Delta\phi\}$, which is a subset of Θ . The remaining angle, ϕ_2 , is redundant given ϕ_1 and $\Delta\phi$; we choose to work with $\Delta\phi$ as it is relevant for SORs. As an intermediate step, we first reweight the posterior samples for each event to account for known astrophysical constraints on the primary mass and mass ratio ($q = m_2/m_1$) populations [9]. The details of the reweighting procedure are given in the Supplement [38]. Post reweighting, Eq. (1) can be rewritten as:

$$p(\Theta|d, R) \propto \mathcal{L}(d|\Theta) \pi(\Theta|R), \quad (2)$$

where R indicates that these are the reweighted posteriors. Using these reweighted posteriors in Eq. (4) below ensures that the implicit priors on the mass population are astrophysically motivated [39].

To constrain the astrophysical distribution of \mathbb{S} , we begin by making the assumption that the true value of \mathbb{S} for each event is drawn from a common underlying distribution $\pi(\mathbb{S}|\Lambda)$, which is conditional on a set of *hyperparameters* Λ . We then use hierarchical Bayesian inference [36] to collectively analyze all 31 events and constrain Λ :

$$p(\Lambda|\{d_i\}) \propto \mathcal{L}(\{d_i\}|\Lambda) \pi(\Lambda), \quad (3)$$

where $p(\Lambda|\{d_i\})$ is the *hyper-posterior* distribution for Λ given a set of observations $\{d_i\}$, $\mathcal{L}(\{d_i\}|\Lambda)$ is the *hyper-likelihood* of this dataset given Λ , and $\pi(\Lambda)$ is the *hyper-prior* distribution for Λ . In our case, $\{d_i\}$ with $i = 1 \dots N$ represents the observed data for our set of $N = 31$ GW events. The hyper-likelihood is obtained by coherently combining the data from from all events [36]:

$$\mathcal{L}(\{d_i\}|\Lambda) \propto \prod_i^N \int d\mathbb{S}_i p(\mathbb{S}_i|d_i, R) \frac{\pi(\mathbb{S}_i|\Lambda)}{\pi(\mathbb{S}_i|R)}. \quad (4)$$

For the underlying distribution $\pi(\mathbb{S}|\Lambda)$, the spin magnitudes and tilts are modeled following the “Default spin” model of Ref. [9]. The orbital-plane spin angles ϕ_1 and $\Delta\phi$ are modeled as being drawn from independent von Mises distributions [40]. The von Mises distribution is an approximation of a Gaussian distribution with periodic boundary conditions and is parameterized by a mean and a standard deviation (or simply, width).

The explicit forms of $\pi(\mathbb{S}|\Lambda)$ and the hyper-prior $\pi(\Lambda)$ are given in the Supplement [38]. In particular, the priors on the mean (μ_{ϕ_1} and $\mu_{\Delta\phi}$) and width (σ_{ϕ_1} and $\sigma_{\Delta\phi}$) hyperparameters for the ϕ_1 and $\Delta\phi$ distributions are as follows. The prior for the mean parameters is always uniform in $(-\pi, \pi)$. We consider two different prior choices for the widths: (i) A Jeffreys prior [41] that is log-uniform in σ_{ϕ_1} and $\sigma_{\Delta\phi}$ between $(0.3, 4\pi)$, henceforth referred to as the *Jeffreys- σ_ϕ* prior. (ii) A prior that is uniform in σ_{ϕ_1} and $\sigma_{\Delta\phi}$ between $(0.3, 4\pi)$, henceforth referred to as

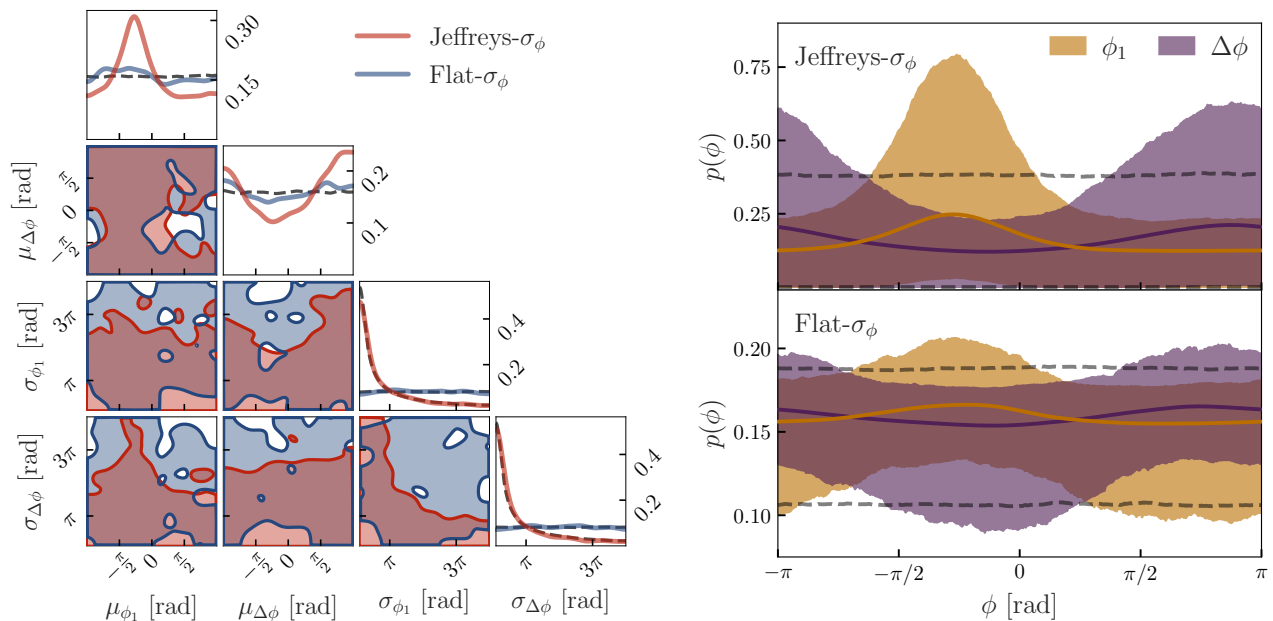


Figure 2. Constraints on the ϕ_1 and $\Delta\phi$ populations at $t_{\text{ref}}/M = -100$. *Left*: Posteriors for the mean and width parameters. The shaded regions show 90% credible bounds on joint 2D posteriors. The diagonal plots show 1D marginalized posteriors, with the priors shown as dashed black lines. We consider two prior choices (**Jeffreys- σ_ϕ** and **Flat- σ_ϕ**) for the width parameters. *Right*: Constraints on the posterior population distributions $p(\phi_1)$ and $p(\Delta\phi)$ for the two prior choices. Shaded regions show 90% credible bounds, while the solid lines show the mean. The dashed grey lines show the 90% prior bounds.

the **Flat- σ_ϕ** prior. The Jeffreys prior is an uninformative prior choice often used for scale parameters [41]. The flat prior may be considered a control case to understand the impact of the prior. The lower limit of 0.3 rad on the width priors is arbitrary, but chosen to be smaller than the sharpest features we expect to be resolvable with LIGO-Virgo (which we estimate from the NR injections in Ref. [30]). The upper limit of 4π is chosen to be large enough to approximate a flat distribution between $(-\pi, \pi)$.

We use the **Bilby** [42] package with the **dynesty** [43] sampler to draw posterior samples for the hyperparameters Λ from $p(\Lambda|\{d_i\})$. Finally, the posterior distribution for the \mathbb{S} population, also referred to as the *posterior population distribution*, is obtained by averaging over Λ [36]:

$$p(\mathbb{S}) = \int d\Lambda \pi(\mathbb{S}|\Lambda) p(\Lambda|\{d_i\}). \quad (5)$$

In practice, this is done by drawing samples from the hyper-posterior $p(\Lambda|\{d_i\})$ and evaluating $\pi(\mathbb{S}|\Lambda)$ on an array of \mathbb{S} values for each Λ sample. This gives us an ensemble of probability distributions on \mathbb{S} , which we use to compute the mean and 90% credible widths. Finally, we note that we ignore selection effects for the spin population, as they are not expected to be significant at current sensitivity [38].

Spin population.— Figure 2 shows our constraints on the ϕ_1 and $\Delta\phi$ populations. The left panel shows the posteriors for the mean and width hyperparameters. For

both **Jeffreys- σ_ϕ** and **Flat- σ_ϕ** prior choices, we find that the 1D marginalized posteriors for the widths σ_{ϕ_1} and $\sigma_{\Delta\phi}$ are dominated by the prior itself. However, the 1D posteriors for the mean parameters show a preference for $\mu_{\phi_1} \sim -\pi/4$ and $\mu_{\Delta\phi} \sim \pm\pi$. This is reflected in the corresponding constraints on the posterior population distributions, $p(\phi_1)$ and $p(\Delta\phi)$, shown in the right panel of Fig. 2. These represent our constraints on the astrophysical distributions for ϕ_1 and $\Delta\phi$; they are generated by evaluating the von Mises model using draws from the joint posterior of the mean and width parameters.

We interpret the population constraint in Fig. 2 as follows. For the **Flat- σ_ϕ** prior, examining the 2D posterior for $\mu_{\Delta\phi} - \sigma_{\Delta\phi}$, we note that when $\sigma_{\Delta\phi} \rightarrow 0$, only the region around $\mu_{\Delta\phi} \sim \pm\pi$ is allowed in the 90% credible region. This means that, if there is a sharp peak in the $\Delta\phi$ population, it is only allowed near $\sim \pm\pi$. Similarly, examining the 2D posterior for $\mu_{\phi_1} - \sigma_{\phi_1}$, we find that when $\sigma_{\phi_1} \rightarrow 0$, there is a preference for $\mu_{\phi_1} \sim -\pi/4$. The preferences in the 1D $\mu_{\phi_1}/\mu_{\Delta\phi}$ posteriors and the $p(\phi_1)/p(\Delta\phi)$ distributions get amplified for the **Jeffreys- σ_ϕ** prior, as this prior already prefers small widths. In short, the data disfavor peaks at regions other than $\phi_1 \sim -\pi/4$ and $\Delta\phi \sim \pm\pi$, and this leads to $p(\phi_1)$ and $p(\Delta\phi)$ peaks in these regions. However, the data are not informative enough to constrain the widths of these peaks. We further note that both populations are still consistent with a uniform distribution at the 90% credible level.

It is important to recognize that the location of the ϕ_1 peak in Fig. 2 depends strongly on our choice of reference

point. This is because ϕ_1 changes on the orbital timescale as it is defined with respect to the line-of-separation (cf. Fig. 1). On the other hand, $\Delta\phi$ only changes on the longer precession time scale, and we find that repeating our analysis using spins measured at 20Hz leads to consistent results for the $\Delta\phi$ population [38]. However, the biggest gain in measuring the spins at $t_{\text{ref}}/M = -100$ is in the ϕ_1 population constraint, as ϕ_1 is significantly better measured there [30]. Constraining both ϕ_1 and $\Delta\phi$ is necessary to constrain the kick population below.

For completeness, we include our constraints on the spin magnitude and tilt populations, along with full model hyperparameter posteriors in the Supplement [38]. Our constraints on the spin magnitude and tilt populations are consistent with Ref. [9], and we do not find any obvious correlations between the orbital-plane spin angles and the other spin parameters. To gain further confidence in our results, we also conduct some mock population studies [38], which suggest that at least some ϕ_1 and $\Delta\phi$ populations can be reliably recovered at current detector sensitivity. Finally, by iteratively leaving one event out from the dataset and repeating our analysis, we check that our results are not driven by any single event.

One limitation of this work is the restriction to the 31 signals with $M \gtrsim 60M_\odot$ so that we can use the `NRSur7dq4` model. We also repeat our analysis for all 46 binary BH events from GWTC-2, using the phenomenological waveform model `IMRPhenomTPHM` [44] for the remaining 15 events. Interestingly, we find that there is some information gain in the width parameters in this case, with a preference for small widths. However, as noted in Ref. [30], `IMRPhenomTPHM` can have biases in recovering the orbital-plane spin angles. Therefore, while we include these results in the Supplement [38] for completeness, we treat Fig. 2 as our main result.

Kick population.— Having constrained the full spin degrees of freedom for the binary BH population, we can now derive constraints on the kick population. We begin by generating one realization of the q , χ_1 and χ_2 populations. For q , we use the same model that was used in the initial posterior reweighting. For $\chi_{1,2}$, we use the spin population constraints at $t_{\text{ref}}/M = -100$. We simply draw one hyperparameter sample from the posterior of the hierarchical analysis and evaluate the q , χ_1 and χ_2 population models at that point. Next, we draw a large number of samples for q , χ_1 and χ_2 from this population realization and compute the corresponding kick magnitudes using the `NRSur7dq4Remnant` model [37, 45]. Repeating these steps over many draws of q , χ_1 and χ_2 populations, we generate an ensemble of kick population distributions $p(v_f)$. For comparison, we also evaluate the prior $p(v_f)$ by repeating this procedure using prior hyperparameter samples.

Figure 3 shows the 90% credible constraints on $p(v_f)$ for the `Jeffreys- σ_ϕ` and `Flat- σ_ϕ` prior choices. In addition, we consider a prior choice where the ϕ_1 and $\Delta\phi$ populations are restricted to be uniformly distributed. We refer to this prior choice as `Infinite- σ_ϕ` , as the other priors

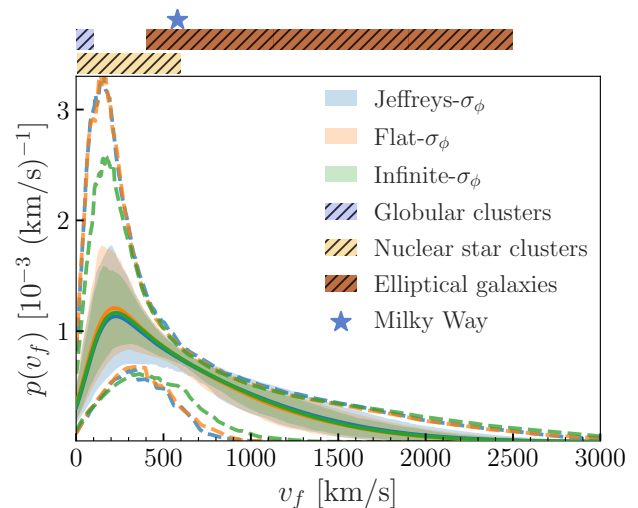


Figure 3. Constraints on the kick magnitude population for different prior choices for σ_{ϕ_1} and $\sigma_{\Delta\phi}$. Shaded regions show the central 90% credible bounds for the posterior, while the solid lines show the mean. The dashed lines show the 90% bounds for the prior. For comparison, we show known ranges for the escape velocities for various types of host environments.

reduce to this when $\sigma_{\phi_1} = \sigma_{\Delta\phi} = \infty$. This restricted prior was also used in Ref. [46] to constrain the kick population. The mass ratio, spin magnitude and tilt population models are the same for all three choices. We compare our kick population constraints against fiducial escape velocities for globular clusters [47, 48], nuclear star clusters [48], elliptical galaxies [20] and Milky Way-like galaxies [49].

Comparing the prior and posterior ranges in Fig. 3, we note that there is significant information gain about the kick population, even though individual events are largely uninformative about the kick [21]. The three prior choices lead to consistent kick populations in Fig. 3, with the `Infinite- σ_ϕ` prior leading to the tightest constraint. This is expected as the `Infinite- σ_ϕ` prior is a special case of the other two. This is also reflected in the more restrictive $p(v_f)$ prior in Fig. 3 for `Infinite- σ_ϕ` . It is somewhat surprising that the kick population is not hugely influenced by the prior choices on ϕ_1 and $\Delta\phi$ population, even though the kick is known to be very sensitive to these parameters [23]. This is explained by the fact that the ϕ_1 and $\Delta\phi$ distributions in Fig. 2 are still consistent with a uniform distribution at 90% credibility. We expect this to change with future observations.

Astrophysical implications.— While the location of the ϕ_1 peak in Fig. 2 is not particularly important, the fact that there is a peak at all is indeed interesting. This feature has not been predicted for any formation channel. Therefore, our naive expectation is that this peak will get smoothed over as more data are added. However, it will be interesting to see if there are alternative explanations.

On the other hand, the preference for $\Delta\phi \sim \pm\pi$ in Fig. 2 is expected in some formation channels where

SORs [3] are important. In particular, stellar binaries with significant supernova natal kicks and efficient stellar tides can be driven towards these resonances [10, 11]. In the standard scenario where the heavier star becomes the heavier BH, the $\Delta\phi \sim \pm\pi$ resonant mode is expected to be dominant. However, if mass transfer between the two components is significant, a mass-ratio reversal occurs and the $\Delta\phi \sim 0$ mode becomes dominant [10]. Note that the predictions of Refs. [10, 11] are at $f_{\text{ref}} = 20$ Hz, while our best constraints are at $t_{\text{ref}}/M = -100$. However, as $\Delta\phi$ only evolves on the precession timescale, we expect that a preference for $\Delta\phi \sim 0$ or $\pm\pi$ at $f_{\text{ref}} = 20$ Hz leads to a similar preference at $t_{\text{ref}}/M = -100$. It will be interesting to extend the analysis of Refs. [10, 11] to $t_{\text{ref}}/M = -100$, for example, using the spin dynamics of NRSur7dq4 [37].

While our $\Delta\phi$ population constraint can be interpreted as coming from SORs, this does not yet constitute conclusive evidence for them—especially not without a measurement of the width of the distribution to confirm this feature. In addition, consider a binary for which the spin angular momenta in the plane of the orbit perfectly cancel (which requires $\Delta\phi = \pm\pi$). This system will not undergo orbital precession and can approximately mimic a spin-aligned system, as pointed out by Ref. [29]. As a result, a precessing waveform model can sometimes mistake a spin-aligned system for one with $\Delta\phi = \pm\pi$. However, such a binary still undergoes spin precession which can be used to break this degeneracy given sufficient signal-to-noise ratio. A more detailed analysis may be necessary to account for effects of such potential degeneracies on our results.

Finally, as an application of our $p(v_f)$ constraints in Fig. 3, we estimate the fraction of merger remnants that would be retained by various host environments. Assuming a maximum escape velocity $v_{\text{esc}}^{\text{max}} = 100$ km/s for globular clusters [47, 48], 6_{-3}^{+5} (6_{-3}^{+4}) % of the remnants will be retained for the **Jeffreys- σ_ϕ** (**Flat- σ_ϕ**) prior. For nuclear star clusters, assuming $v_{\text{esc}}^{\text{max}} = 600$ km/s [48], the retention fraction is constrained to 54_{-17}^{+19} (57_{-15}^{+16}) % for the **Jeffreys- σ_ϕ** (**Flat- σ_ϕ**) prior. Averaging over the two prior choices, we estimate the retention fraction to be $\sim 3 - 10$ % for globular clusters, and $\sim 39 - 73$ % for nuclear star clusters. All constraints are quoted at 90% credibility. Our constraints on the retention fraction are consistent with those of Refs. [46, 50].

If the observed $\Delta\phi \sim \pm\pi$ preference is confirmed to be due to SORs, our findings have several important implications: (i) SOR measurements can be used to place new astrophysical constraints on supernova natal kicks and stellar tides [10, 11]. (ii) SORs can be used to constrain the cosmic merger rate of isolated stellar binaries in galactic fields, as well as measure what fraction of merging binaries form via that channel. (iii) The $\Delta\phi \sim \pm\pi$ resonance mode tends to enhance merger kicks and suppress the spins of the remnant BHs [51, 52], both of which

are important observables for constraining the formation of heavy BHs via successive mergers [22]. Furthermore, independent of whether our findings can be attributed to SORs, our $p(v_f)$ constraints already suggest that globular clusters are an unlikely site for that formation channel.

Conclusion.— We constrain the distribution of the orbital-plane spin orientations ϕ_1 and $\Delta\phi$ in the binary black hole population. We find that there is a preference for $\Delta\phi \sim \pm\pi$, which can be a signature of SORs. In addition, we find a preference for $\phi_1 \sim -\pi/4$ in the population, which has not been predicted for any astrophysical formation channel. However, the strength of these preferences depends on our prior choices. Finally, we constrain the distribution of recoil kicks in the population, and estimate the fraction of merger remnants retained by globular and nuclear star clusters. We make our population constraints publicly available at Ref. [53].

Observational evidence for SORs has far reaching implications for black hole astrophysics. While our population constraints suggest the influence of SORs, we are unable to constrain the widths of the ϕ_1 and $\Delta\phi$ distributions with the current dataset of events. Therefore, further observations are necessary to confirm these trends. With LIGO and Virgo approaching their design sensitivities [54], our constraints are certain to improve in the near future.

Acknowledgments.— We thank Davide Gerosa and Katerina Chatziioannou for useful discussions. V.V. was supported by a Klarman Fellowship at Cornell. This project has received funding from the European Union’s Horizon 2020 research and innovation programme under the Marie Skłodowska-Curie grant agreement No. 896869. S.B., M.I. and S.V. acknowledge support of the National Science Foundation and the LIGO Laboratory. S.B. is also supported by the NSF Graduate Research Fellowship under Grant No. DGE-1122374. M.I. is supported by NASA through the NASA Hubble Fellowship grant No. HST-HF2-51410.001-A awarded by the Space Telescope Science Institute, which is operated by the Association of Universities for Research in Astronomy, Inc., for NASA, under contract NAS5-26555. This research made use of data, software and/or web tools obtained from the Gravitational Wave Open Science Center [55], a service of the LIGO Laboratory, the LIGO Scientific Collaboration and the Virgo Collaboration. LIGO was constructed by the California Institute of Technology and Massachusetts Institute of Technology with funding from the National Science Foundation and operates under Cooperative Agreement No. PHY-1764464. Computations were performed on the Alice cluster at ICTS; the Nemo cluster at University of Wisconsin-Milwaukee, which is supported by NSF Grant PHY-1626190; the Wheeler cluster at Caltech, which is supported by the Sherman Fairchild Foundation and by Caltech; and the High Performance Cluster at Caltech.

- [1] Theocharis A. Apostolatos, Curt Cutler, Gerald J. Sussman, and Kip S. Thorne, “Spin-induced orbital precession and its modulation of the gravitational waveforms from merging binaries,” *Phys. Rev. D* **49**, 6274–6297 (1994).
- [2] Lawrence E. Kidder, “Coalescing binary systems of compact objects to postNewtonian 5/2 order. 5. Spin effects,” *Phys. Rev. D* **52**, 821–847 (1995), arXiv:gr-qc/9506022.
- [3] Jeremy D. Schnittman, “Spin-orbit resonance and the evolution of compact binary systems,” *Phys. Rev. D* **70**, 124020 (2004), arXiv:astro-ph/0409174.
- [4] Michael Kesden, Davide Gerosa, Richard O’Shaughnessy, Emanuele Berti, and Ulrich Sperhake, “Effective potentials and morphological transitions for binary black-hole spin precession,” *Phys. Rev. Lett.* **114**, 081103 (2015), arXiv:1411.0674 [gr-qc].
- [5] Davide Gerosa, Michael Kesden, Ulrich Sperhake, Emanuele Berti, and Richard O’Shaughnessy, “Multi-timescale analysis of phase transitions in precessing black-hole binaries,” *Phys. Rev. D* **92**, 064016 (2015), arXiv:1506.03492 [gr-qc].
- [6] Davide Gerosa, Richard O’Shaughnessy, Michael Kesden, Emanuele Berti, and Ulrich Sperhake, “Distinguishing black-hole spin-orbit resonances by their gravitational-wave signatures,” *Phys. Rev. D* **89**, 124025 (2014), arXiv:1403.7147 [gr-qc].
- [7] Daniele Trifirò, Richard O’Shaughnessy, Davide Gerosa, Emanuele Berti, Michael Kesden, Tyson Littenberg, and Ulrich Sperhake, “Distinguishing black-hole spin-orbit resonances by their gravitational wave signatures. II: Full parameter estimation,” *Phys. Rev. D* **93**, 044071 (2016), arXiv:1507.05587 [gr-qc].
- [8] Chaitanya Afle *et al.*, “Detection and characterization of spin-orbit resonances in the advanced gravitational wave detectors era,” *Phys. Rev. D* **98**, 083014 (2018), arXiv:1803.07695 [gr-qc].
- [9] R. Abbott *et al.* (LIGO Scientific, Virgo), “Population Properties of Compact Objects from the Second LIGO-Virgo Gravitational-Wave Transient Catalog,” *Astrophys. J. Lett.* **913**, L7 (2021), arXiv:2010.14533 [astro-ph.HE].
- [10] Davide Gerosa, Michael Kesden, Emanuele Berti, Richard O’Shaughnessy, and Ulrich Sperhake, “Resonant-plane locking and spin alignment in stellar-mass black-hole binaries: a diagnostic of compact-binary formation,” *Phys. Rev. D* **87**, 104028 (2013), arXiv:1302.4442 [gr-qc].
- [11] Davide Gerosa, Emanuele Berti, Richard O’Shaughnessy, Krzysztof Belczynski, Michael Kesden, Daniel Wysocki, and Wojciech Gladysz, “Spin orientations of merging black holes formed from the evolution of stellar binaries,” *Phys. Rev. D* **98**, 084036 (2018), arXiv:1808.02491 [astro-ph.HE].
- [12] More precisely, we use the coorbital frame defined in Ref. [37]. In this frame, the z -axis is along the direction that maximises the power in the (2,2) mode, which is taken to be the direction of the orbital angular momentum [56]. The x -axis is along the line of separation from the lighter to the heavier BH, and the y -axis completes the right-handed triad. Note that this frame is defined using the gauge-invariant waveform at future null infinity, rather than the gauge-dependent BH trajectories. ().
- [13] W. B. Bonnor, M. A. Rotenberg, and Rosenhead Louis, “Transport of momentum by gravitational waves: the linear approximation,” *Proceedings of the Royal Society of London Series A* **265** (1961), 10.1098/rspa.1961.0226.
- [14] Asher Peres, “Classical radiation recoil,” *Phys. Rev.* **128**, 2471–2475 (1962).
- [15] Jacob D. Bekenstein, “Gravitational-Radiation Recoil and Runaway Black Holes,” *The Astrophysical Journal* **183**, 657–664 (1973).
- [16] M. J. Fitchett, “The influence of gravitational wave momentum losses on the centre of mass motion of a Newtonian binary system,” *Monthly Notices of the Royal Astronomical Society* **203**, 1049–1062 (1983), <http://oup.prod.sis.lan/mnras/article-pdf/203/4/1049/18223796/mnras203-1049.pdf>.
- [17] Manuela Campanelli, Carlos O. Lousto, Yosef Zlochower, and David Merritt, “Maximum gravitational recoil,” *Phys. Rev. Lett.* **98**, 231102 (2007), arXiv:gr-qc/0702133 [GR-QC].
- [18] J. A. Gonzalez, M. D. Hannam, U. Sperhake, Bernd Bruegmann, and S. Husa, “Supermassive recoil velocities for binary black-hole mergers with antialigned spins,” *Phys. Rev. Lett.* **98**, 231101 (2007), arXiv:gr-qc/0702052 [GR-QC].
- [19] Carlos O. Lousto and Yosef Zlochower, “Hangup Kicks: Still Larger Recoils by Partial Spin/Orbit Alignment of Black-Hole Binaries,” *Phys. Rev. Lett.* **107**, 231102 (2011), arXiv:1108.2009 [gr-qc].
- [20] David Merritt, Milos Milosavljevic, Marc Favata, Scott A. Hughes, and Daniel E. Holz, “Consequences of gravitational radiation recoil,” *Astrophys. J.* **607**, L9–L12 (2004), arXiv:astro-ph/0402057 [astro-ph].
- [21] Vijay Varma, Maximiliano Isi, and Sylvia Biscoveanu, “Extracting the Gravitational Recoil from Black Hole Merger Signals,” *Phys. Rev. Lett.* **124**, 101104 (2020), arXiv:2002.00296 [gr-qc].
- [22] Davide Gerosa and Maya Fishbach, “Hierarchical mergers of stellar-mass black holes and their gravitational-wave signatures,” *Nature Astron.* **5**, 8 (2021), arXiv:2105.03439 [astro-ph.HE].
- [23] Bernd Bruegmann, Jose A. Gonzalez, Mark Hannam, Sascha Husa, and Ulrich Sperhake, “Exploring black hole superkicks,” *Phys. Rev. D* **77**, 124047 (2008), arXiv:0707.0135 [gr-qc].
- [24] J. Aasi *et al.* (LIGO Scientific), “Advanced LIGO,” *Class. Quant. Grav.* **32**, 074001 (2015), arXiv:1411.4547 [gr-qc].
- [25] F. Acernese *et al.* (Virgo), “Advanced Virgo: a second-generation interferometric gravitational wave detector,” *Class. Quant. Grav.* **32**, 024001 (2015), arXiv:1408.3978 [gr-qc].
- [26] B. P. Abbott *et al.* (LIGO Scientific, Virgo), “Binary Black Hole Population Properties Inferred from the First and Second Observing Runs of Advanced LIGO and Advanced Virgo,” *Astrophys. J. Lett.* **882**, L24 (2019), arXiv:1811.12940 [astro-ph.HE].
- [27] Salvatore Vitale, Ryan Lynch, John Veitch, Vivien Raymond, and Riccardo Sturani, “Measuring the spin of black holes in binary systems using gravitational waves,” *Phys. Rev. Lett.* **112**, 251101 (2014), arXiv:1403.0129 [gr-qc].
- [28] P. Schmidt, F. Ohme, and M. Hannam, “Towards models of gravitational waveforms from generic binaries II: Modelling precession effects with a single effective pre-

- cession parameter,” *Phys. Rev. D* **91**, 024043 (2015), arXiv:1408.1810 [gr-qc].
- [29] Sylvia Biscoveanu, Maximiliano Isi, Vijay Varma, and Salvatore Vitale, “Measuring the spins of heavy binary black holes,” (2021), arXiv:2106.06492 [gr-qc].
- [30] Vijay Varma, Maximiliano Isi, Sylvia Biscoveanu, Will M. Farr, and Salvatore Vitale, “Measuring binary black hole orbital-plane spin orientations,” *Phys. Rev. D* **105**, 024045 (2022), arXiv:2107.09692 [astro-ph.HE].
- [31] R. Abbott *et al.* (LIGO Scientific, Virgo), “GWTC-2: Compact Binary Coalescences Observed by LIGO and Virgo During the First Half of the Third Observing Run,” *Phys. Rev. X* **11**, 021053 (2021), arXiv:2010.14527 [gr-qc].
- [32] B. P. Abbott *et al.* (LIGO Scientific, Virgo), “GWTC-1: A Gravitational-Wave Transient Catalog of Compact Binary Mergers Observed by LIGO and Virgo during the First and Second Observing Runs,” *Phys. Rev. X* **9**, 031040 (2019), arXiv:1811.12907 [astro-ph.HE].
- [33] Rich Abbott *et al.* (LIGO Scientific, Virgo), “Open data from the first and second observing runs of Advanced LIGO and Advanced Virgo,” *SoftwareX* **13**, 100658 (2021), arXiv:1912.11716 [gr-qc].
- [34] LIGO Scientific Collaboration and Virgo Collaboration, “GWTC-1,” <https://doi.org/10.7935/82H3-HH23> (2018).
- [35] LIGO Scientific Collaboration and Virgo Collaboration, “GWTC-2,” <https://doi.org/10.7935/99gf-ax93> (2020).
- [36] Eric Thrane and Colm Talbot, “An introduction to Bayesian inference in gravitational-wave astronomy: Parameter estimation, model selection, and hierarchical models,” *Publications of the Astronomical Society of Australia* **36**, e010 (2019), arXiv:1809.02293 [astro-ph.IM].
- [37] Vijay Varma, Scott E. Field, Mark A. Scheel, Jonathan Blackman, Davide Gerosa, Leo C. Stein, Lawrence E. Kidder, and Harald P. Pfeiffer, “Surrogate models for precessing binary black hole simulations with unequal masses,” *Phys. Rev. Research* **1**, 033015 (2019), arXiv:1905.09300 [gr-qc].
- [38] See Supplemental Material [here](#), for details about our hierarchical analysis, posterior for the full spin population, population constraints at 20 Hz, a mock population study, and results for all GWTC-2 events (using a phenomenological model when the surrogate is not applicable). This further includes Refs. [57–66] ().
- [39] Salvatore Vitale, Davide Gerosa, Will M. Farr, and Stephen R. Taylor, “Inferring the properties of a population of compact binaries in presence of selection effects,” (2020), arXiv:2007.05579 [astro-ph.IM].
- [40] K. V. Mardia and P. E. Jupp, *Directional Statistics* (John Wiley and Sons, Ltd., West Sussex, 1999).
- [41] Harold Jeffreys, “An Invariant Form for the Prior Probability in Estimation Problems,” *Proceedings of the Royal Society of London Series A* **186**, 453–461 (1946).
- [42] Gregory Ashton *et al.*, “BILBY: A user-friendly Bayesian inference library for gravitational-wave astronomy,” *Astrophys. J. Suppl.* **241**, 27 (2019), arXiv:1811.02042 [astro-ph.IM].
- [43] Joshua S. Speagle, “DYNESTY: a dynamic nested sampling package for estimating Bayesian posteriors and evidences,” *Monthly Notices of the Royal Astronomical Society* **493**, 3132–3158 (2020), arXiv:1904.02180 [astro-ph.IM].
- [44] Héctor Estellés, Marta Colleoni, Cecilio García-Quirós, Sascha Husa, David Keitel, Maite Mateu-Lucena, Maria de Lluc Planas, and Antoni Ramos-Buades, “New twists in compact binary waveform modelling: a fast time domain model for precession,” (2021), arXiv:2105.05872 [gr-qc].
- [45] Vijay Varma, Davide Gerosa, Leo C. Stein, François Hébert, and Hao Zhang, “High-accuracy mass, spin, and recoil predictions of generic black-hole merger remnants,” *Phys. Rev. Lett.* **122**, 011101 (2019), arXiv:1809.09125 [gr-qc].
- [46] Zoheyr Doctor, Ben Farr, and Daniel E. Holz, “Black Hole Leftovers: The Remnant Population from Binary Black Hole Mergers,” *Astrophys. J. Lett.* **914**, L18 (2021), arXiv:2103.04001 [astro-ph.HE].
- [47] Oleg Y. Gnedin, HongSheng Zhao, J. E. Pringle, S. Michael Fall, Mario Livio, and Georges Meylan, “The unique history of the globular cluster omega centauri,” *Astrophys. J. Lett.* **568**, L23–L26 (2002), arXiv:astro-ph/0202045.
- [48] Fabio Antonini and Frederic A. Rasio, “Merging black hole binaries in galactic nuclei: implications for advanced-LIGO detections,” *Astrophys. J.* **831**, 187 (2016), arXiv:1606.04889 [astro-ph.HE].
- [49] G. Monari, B. Famaey, I. Carrillo, T. Piffl, M. Steinmetz, R. F. G. Wyse, F. Anders, C. Chiappini, and K. Janßen, “The escape speed curve of the Galaxy obtained from Gaia DR2 implies a heavy Milky Way,” *A&A* **616**, L9 (2018), arXiv:1807.04565 [astro-ph.GA].
- [50] Parthapratim Mahapatra, Anuradha Gupta, Marc Favata, K. G. Arun, and B. S. Sathyaprakash, “Remnant Black Hole Kicks and Implications for Hierarchical Mergers,” *Astrophys. J. Lett.* **918**, L31 (2021), arXiv:2106.07179 [astro-ph.HE].
- [51] Emanuele Berti, Michael Kesden, and Ulrich Sperhake, “Effects of post-Newtonian Spin Alignment on the Distribution of Black-Hole Recoils,” *Phys. Rev.* **D85**, 124049 (2012), arXiv:1203.2920 [astro-ph.HE].
- [52] Michael Kesden, Ulrich Sperhake, and Emanuele Berti, “Relativistic Suppression of Black Hole Recoils,” *Astrophys. J.* **715**, 1006–1011 (2010), arXiv:1003.4993 [astro-ph.CO].
- [53] Vijay Varma, Sylvia Biscoveanu, Maximiliano Isi, Will M. Farr, and Salvatore Vitale, “Public data release for “Hints of spin-orbit resonances in the binary black hole population.”,” github.com/vijayvarma392/spin_kick_pop_GWTC2.
- [54] B. P. Abbott *et al.* (KAGRA, LIGO Scientific, VIRGO), “Prospects for Observing and Localizing Gravitational-Wave Transients with Advanced LIGO, Advanced Virgo and KAGRA,” *Living Rev. Rel.* **21**, 3 (2018), arXiv:1304.0670 [gr-qc].
- [55] LIGO Scientific Collaboration and Virgo Collaboration, “Gravitational Wave Open Science Center,” <https://www.gw-openscience.org>.
- [56] Michael Boyle, Robert Owen, and Harald P. Pfeiffer, “A geometric approach to the precession of compact binaries,” *Phys. Rev.* **D84**, 124011 (2011), arXiv:1110.2965 [gr-qc].
- [57] Shanika Galadage, Colm Talbot, and Eric Thrane, “Gravitational-wave inference in the catalog era: evolving priors and marginal events,” *Phys. Rev. D* **102**, 083026 (2020), arXiv:1912.09708 [astro-ph.HE].
- [58] I. M. Romero-Shaw *et al.*, “Bayesian inference for compact binary coalescences with bilby: validation and application to the first LIGO–Virgo gravitational-wave transient catalogue,” *Mon. Not. Roy. Astron. Soc.* **499**, 3295–3319 (2020), arXiv:2006.00714 [astro-ph.IM].

- [59] Daniel Wysocki, Jacob Lange, and Richard O’Shaughnessy, “Reconstructing phenomenological distributions of compact binaries via gravitational wave observations,” *Phys. Rev. D* **100**, 043012 (2019), [arXiv:1805.06442 \[gr-qc\]](#).
- [60] Colm Talbot and Eric Thrane, “Determining the population properties of spinning black holes,” *Phys. Rev. D* **96**, 023012 (2017), [arXiv:1704.08370 \[astro-ph.HE\]](#).
- [61] R. Abbott *et al.* (LIGO Scientific, Virgo), “GW190521: A Binary Black Hole Merger with a Total Mass of $150 M_{\odot}$,” *Phys. Rev. Lett.* **125**, 101102 (2020), [arXiv:2009.01075 \[gr-qc\]](#).
- [62] J. Veitch *et al.*, “Robust parameter estimation for compact binaries with ground-based gravitational-wave observations using the LALInference software library,” *Phys. Rev. D* **91**, 042003 (2015), [arXiv:1409.7215 \[gr-qc\]](#).
- [63] Vijay Varma, Scott E. Field, Mark A. Scheel, Jonathan Blackman, Lawrence E. Kidder, and Harald P. Pfeiffer, “Surrogate model of hybridized numerical relativity binary black hole waveforms,” *Phys. Rev. D* **99**, 064045 (2019), [arXiv:1812.07865 \[gr-qc\]](#).
- [64] Kashif Alvi, “Energy and angular momentum flow into a black hole in a binary,” *Phys. Rev. D* **64**, 104020 (2001), [arXiv:gr-qc/0107080](#).
- [65] Eric Poisson, “Absorption of mass and angular momentum by a black hole: Time-domain formalisms for gravitational perturbations, and the small-hole / slow-motion approximation,” *Phys. Rev. D* **70**, 084044 (2004), [arXiv:gr-qc/0407050](#).
- [66] Jonathan Blackman, Scott E. Field, Mark A. Scheel, Chad R. Galley, Christian D. Ott, Michael Boyle, Lawrence E. Kidder, Harald P. Pfeiffer, and Béla Szilágyi, “Numerical relativity waveform surrogate model for generically precessing binary black hole mergers,” *Phys. Rev. D* **96**, 024058 (2017), [arXiv:1705.07089 \[gr-qc\]](#).

SUPPLEMENTAL MATERIALS

I. ADDITIONAL DETAILS ON THE HIERARCHICAL ANALYSIS

In this section, we provide additional details on the reweighting procedure applied to posterior samples for individual GW events, the explicit forms for the spin population model and the hyper-prior, and potential selection effects in the hierarchical analysis.

A. Reweighting to an astrophysical mass, mass ratio, and redshift prior

We are interested in constraining the population for the full spin degrees of freedom, $\mathbb{S} = \{\chi_1, \chi_2, \theta_1, \theta_2, \phi_1, \Delta\phi\}$ (cf. Fig. 1). Recently, Ref. [9] analyzed the GWTC-2 catalog to place constraints on the populations of component BH masses, spin magnitudes and tilts (but not ϕ_1 and $\Delta\phi$). For simplicity, we only model the spin degrees of freedom in this work, but incorporate the astrophysical mass and mass-ratio population constraints from Ref. [9].

We denote $\Gamma = \{m_1^{\text{src}}, q\}$, where $m_1^{\text{src}} = m_1/(1+z)$ is the mass of the heavier BH in the source frame, and z is the source redshift. To account for the astrophysical constraints on Γ , we apply the following weights to the posterior samples for each individual event

$$w(\Gamma_j) = \frac{p(\Gamma_j | \{d\}_{i \neq j})}{\pi(\Gamma_j)}, \quad (\text{S1})$$

where j indicates the particular GW event, $\pi()$ is the same prior as in Eq. (1), and $p(\Gamma_j | \{d\}_{i \neq j})$ denotes the posterior population distribution (cf. Eq. (46) of Ref. [57]) for the Γ population obtained using the data from all events other than j . We use the public data release for the ‘‘Power Law + Peak’’ model from Ref. [9] for the Γ population constraints. $p(\Gamma_j | \{d\}_{i \neq j})$ is obtained from these results using the ‘‘leave-one-out’’ computation described in Ref. [57]. This ensures that the event j is not double-counted in the analysis.

We perform an additional reweighting to switch to a more astrophysically motivated redshift prior. Note that, when obtaining the posterior samples in Eq. (1), Ref. [30] used a prior that is uniform in comoving volume [31, 58]:

$$\pi(z) \propto \frac{dV_c}{dz}, \quad (\text{S2})$$

where dV_c/dz is the differential comoving volume. We now apply the weights

$$w(z_j) = (1+z_j)^{-1}. \quad (\text{S3})$$

to these posteriors, effectively switching to a prior that that is uniform in comoving volume *and* source frame time [31, 58]:

$$\pi(z) \propto \frac{dV_c}{dz} (1+z)^{-1}. \quad (\text{S4})$$

The additional $(1+z)^{-1}$ factor accounts for cosmological time dilation. This matches the redshift prior assumed for the ‘‘Power Law + Peak’’ model in Ref. [9]. We perform both reweighting steps simultaneously, by applying the weights

$$w(\Theta_j) = w(\Gamma_j) w(z_j), \quad (\text{S5})$$

to the posterior samples Θ_j for each event j in our dataset. Post reweighting, Eq. (1) can be rewritten as Eq. (2).

Note that Ref. [9] models the mass degrees of freedom simultaneously with the spin degrees of freedom. Using the mass-population-reweighted posteriors is equivalent to Ref. [9], except that this does not account for any possible correlations between the mass and spin hyperparameters. However, Ref. [9] found that these correlations are not significant.

Parameter	Prior
μ_χ	U(0, 1)
σ_χ^2	U(0, 0.25)
ξ_θ	U(0,1)
σ_θ	U(0.01,4)
μ_{ϕ_1}	U($-\pi, \pi$)
$\mu_{\Delta\phi}$	U($-\pi, \pi$)
σ_{ϕ_1}	See Tab. S2.
$\sigma_{\Delta\phi}$	See Tab. S2.

Table S1. Priors on hyperparameters for our spin population model. In addition, following Ref. [9], we exclude μ_χ, σ_χ^2 values where the Beta distribution becomes singular. Here, $U(a, b)$ indicates a uniform distribution on the interval (a, b) .

Name	Prior on σ_{ϕ_1} and $\sigma_{\Delta\phi}$
Jeffreys-σ_ϕ	LU(0.3, 4π)
Flat-σ_ϕ	U(0.3, 4π)
Infinite-σ_ϕ	$\delta(\infty)$

Table S2. The prior choices we consider for σ_{ϕ_1} and $\sigma_{\Delta\phi}$. LU(a, b) indicates a log-uniform distribution on the interval (a, b) , while $\delta(a)$ indicates a Dirac delta distribution where the parameter is fixed at a . Note that the **Infinite- σ_ϕ** prior restricts the ϕ_1 and $\Delta\phi$ populations to be uniform.

B. Population model

We use the following joint distribution for the underlying spin distribution $\pi(\mathbb{S}|\Lambda)$ in Eq. (4):

$$\pi(\mathbb{S}|\Lambda) = p(\chi_{1,2} | \mu_\chi, \sigma_\chi^2) p(\theta_{1,2} | \xi_\theta, \sigma_\theta) p(\phi_1 | \mu_{\phi_1}, \sigma_{\phi_1}) p(\Delta\phi | \mu_{\Delta\phi}, \sigma_{\Delta\phi}). \quad (\text{S6})$$

Here, $p(\chi_{1,2} | \mu_\chi, \sigma_\chi^2)$ is a Beta distribution in the spin magnitudes, parameterized by its mean μ_χ and variance σ_χ^2 [59], and $p(\theta_{1,2} | \xi_\theta, \sigma_\theta)$ is an isotropic tilt distribution

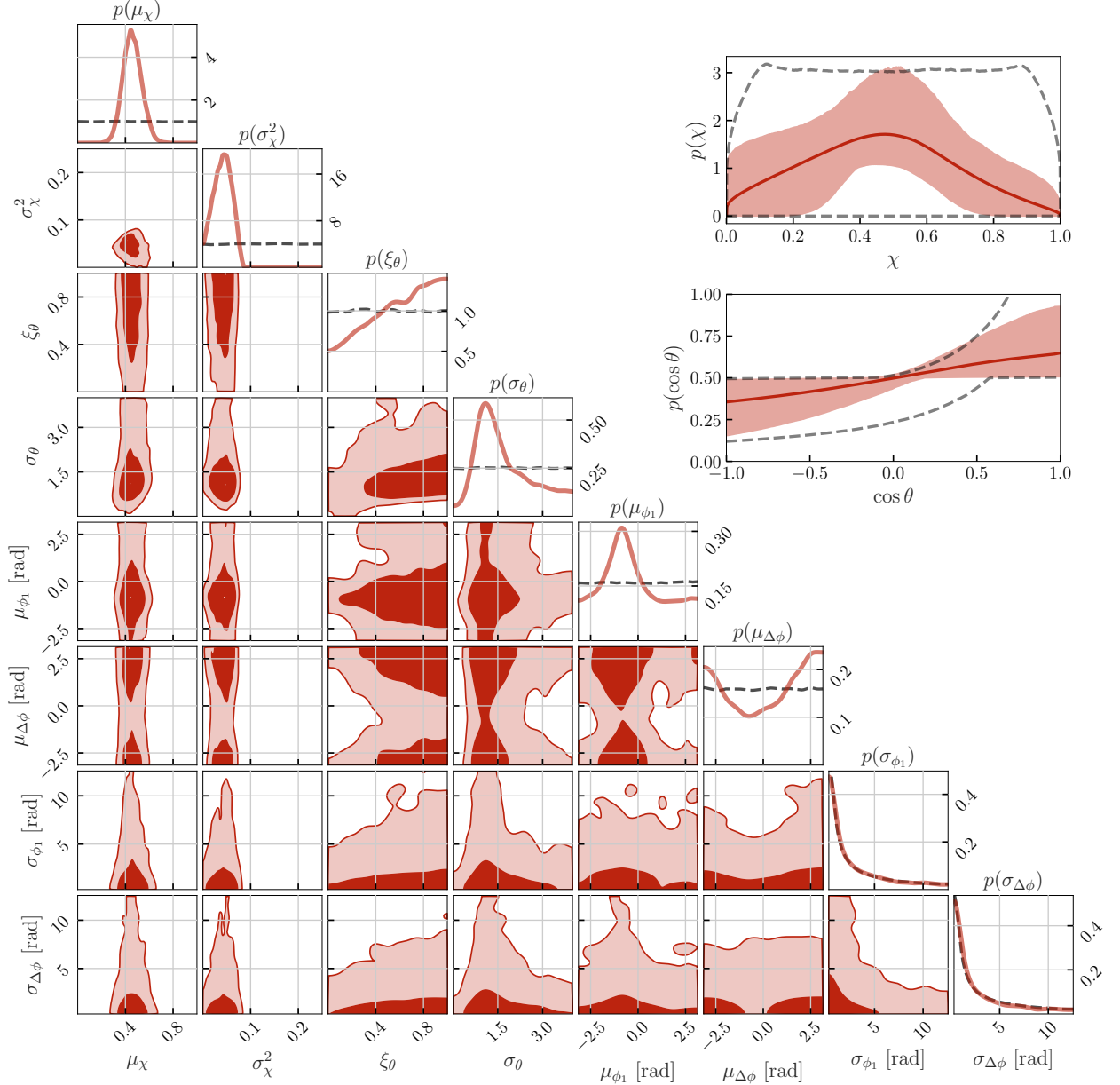


Figure S1. Posterior distribution for hyperparameters for our spin model with a Jeffreys prior for σ_{ϕ_1} and $\sigma_{\Delta\phi}$. The shaded regions in the lower-triangle subplots represent 50% and 90% credible bounds on joint 2D posteriors. The diagonal subplots show the 1D marginalized posteriors and priors (black dashed lines). In the top-right, we show constraints on the spin magnitude and tilt populations. Shaded regions show the central 90% credible bounds, while the solid lines show the mean. The dashed grey lines show the 90% prior bounds. The corresponding population constraints on ϕ_1 and $\Delta\phi$ are shown in the top half of the right-panel of Fig. 2.

with a Gaussian peak component, parameterized by the standard deviation σ_θ of the Gaussian and the mixing fraction ξ_θ coming from the Gaussian component [60]. Note that we assume the distributions for the two component BHs are the same for the spin magnitude and tilt. This model for the spin magnitudes and tilts is the same as “Default spin” model described in App.D.1 of Ref. [9]. On top of this model, we include $p(\phi_1 | \mu_{\phi_1}, \sigma_{\phi_1})$ and $p(\Delta\phi | \mu_{\Delta\phi}, \sigma_{\Delta\phi})$ as independent von Mises distri-

butions parameterized by their corresponding mean and standard deviations. Our choices for the hyper-prior $\pi(\Lambda)$ (cf. Eq. (3)) imposed on the hyperparameters are described in Tab. S1.

The von Mises distribution [40] is defined as

$$p(\phi | \mu, \kappa) = \frac{\exp(\kappa \cos(\phi - \mu))}{2\pi I_0(\kappa)}, \quad (\text{S7})$$

where μ is the mean, κ is a shape parameter, and I_0 is

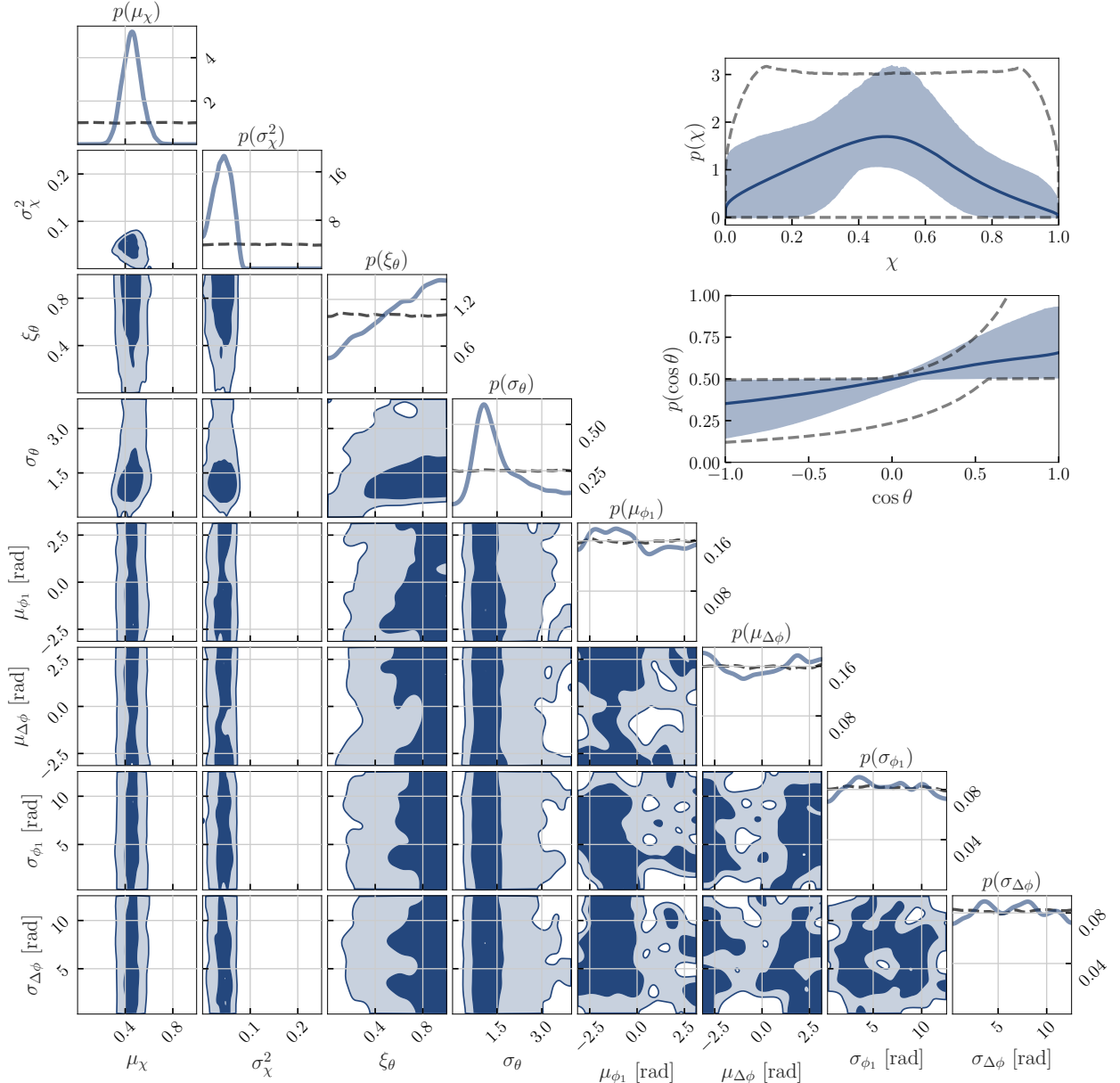


Figure S2. Same as Fig. S1, but using a Flat prior for σ_{ϕ_1} and $\sigma_{\Delta\phi}$. The corresponding ϕ_1 and $\Delta\phi$ population constraints are shown in the bottom half of the right-panel of Fig. 2.

the modified Bessel function of order 0. The von Mises distribution is a close approximation of a Gaussian with periodic boundary conditions at $\phi = \pm\pi$, making it an appropriate choice for phase parameters like ϕ_1 and $\Delta\phi$. The variance of the von Mises distribution can be approximated as $1/\kappa$; therefore we define the standard deviation to be $\sigma \equiv 1/\sqrt{\kappa}$.

C. Selection effects

Ref. [9] also distinguishes between the *astrophysical* distribution of a parameter—the distribution

as it is in nature—and the *observed* distribution of a parameter—the distribution as it appears among detected events due to selection effects, because of which binaries with certain parameters may be easier to detect than others. These effects can be accounted for by modifying the hyper-likelihood in Eq. (4) as done in Eq. (1) of Ref. [9]. While Ref. [9] includes selection effects for their mass population models, they are ignored for the “Default spin” model as they are not expected to be significant at current detector sensitivity.

In our case, the mass-reweighted posteriors (cf. Sec. IA) already account for selection effects for the mass population. As we simply extend the spin population model

of Ref. [9] with the ϕ_1 and $\Delta\phi$ models, we also ignore selection effects for our spin population model. As noted in Ref. [9], it will be important to include spin selection effects as detectors sensitivity improves. However, at current sensitivity, assuming spin selection effects are not significant (as done in Ref. [9]), our results can be treated as constraints on the astrophysical distribution rather than the observed distribution.

Additional selection effects can arise from the NRSur7dq4 requirement of $M \gtrsim 60M_\odot$, which restricts us to 31 of the available 46 events in GWTC-2. However, assuming the correlations between the mass and spin population distributions are not significant at current sensitivity [9], imposing an additional selection criterion on the masses should not affect the inferred spin distribution, as the 31 events included in our analysis would be a fair representation of the underlying spin distribution. Note that while Ref. [9] found that such correlations are not significant, this did not include the orbital-plane spin angles. Therefore, a full resolution of this would require extending NRSur7dq4 to longer inspirals; see Ref. [63] for work in this direction. Finally, NRSur7dq4 is also restricted to mass ratios $q \geq 1/6$ [37]. However, this restriction does not exclude any additional events, as the only GWTC-2 events with significant support at $q \lesssim 1/6$ also have a total mass $< 60M_\odot$ [31].

II. ADDITIONAL INVESTIGATIONS

A. Full spin population

In Fig. 2, we only show the population constraints on ϕ_1 and $\Delta\phi$. For completeness, we now show the hyperparameter posteriors and population constraints on the spin magnitudes and tilts in Fig. S1 (for the **Jeffreys- σ_ϕ** prior) and Fig. S2 (for the **Flat- σ_ϕ** prior). Our population constraints on the spin magnitudes and tilts are consistent with Ref. [9], but somewhat broader as we only use 31 of the available 46 binary BH events in GWTC-2. We do not find any clear correlations between the orbital-plane spin angles and the other spin parameters.

The spin magnitude and tilt populations of Ref. [9] are constrained at $f_{\text{ref}} = 20$ Hz while our constraints are at $t_{\text{ref}}/M = -100$. However, we expect these populations to be similar, as spin tilt measurements at current detector sensitivity are not strongly dependent on the reference point [30]. While the BH spin magnitudes can evolve during the inspiral due to in-falling angular momentum carried by GWs, this is a very small effect (4PN higher than leading angular-momentum loss [64, 65]), and is thus safely ignored by current waveform models including NRSur7dq4. The orbital-plane spin angle measurements, on the other hand, do strongly depend on the reference point [30], which leads to noticeable differences in the population constraints as discussed in Sec. II B.

B. Population constraints at $f_{\text{ref}} = 20$ Hz

The results in Fig. 2 are obtained using NRSur7dq4 spin posteriors at $t_{\text{ref}}/M = -100$ [30]. Ref. [30] also generated NRSur7dq4 spin posteriors at $f_{\text{ref}} = 20$ Hz. In this section, we repeat our hierarchical analysis using these spin posteriors for comparison. Figure S3 shows constraints on the ϕ_1 and $\Delta\phi$ populations when spins are measured at $f_{\text{ref}} = 20$ Hz. Because the $\Delta\phi$ measurements for individual events do not change significantly between $f_{\text{ref}} = 20$ Hz and $t_{\text{ref}}/M = -100$ (cf. Fig. 4 of Ref. [30]), the $\Delta\phi$ populations are also consistent between Fig. S3 and Fig. 2. By contrast, as there is significant improvement in ϕ_1 measurements for individual events at $t_{\text{ref}}/M = -100$ (cf. Fig. 3 of Ref. [30]), the ϕ_1 population is much better constrained in Fig. 2 compared to Fig. S3. It is important to note that this does not imply that the astrophysical ϕ_1 distribution is flatter at $f_{\text{ref}} = 20$ Hz compared to $t_{\text{ref}}/M = -100$. Instead, this is because the ϕ_1 measurements at $f_{\text{ref}} = 20$ Hz are very poor. In fact, even the mild peak near $\phi_1 \sim 0$ for the **Jeffreys- σ_ϕ** prior in Fig. S3 is driven entirely by GW190521 [61]. As discussed in Ref. [30], GW190521 is the only event with a good measurement of ϕ_1 at $f_{\text{ref}} = 20$ Hz as this binary happens to merge near 20 Hz.

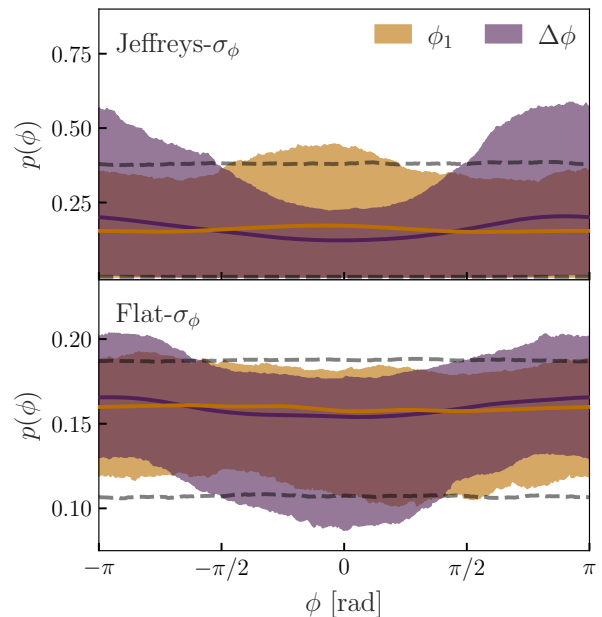


Figure S3. Same as Fig. 2, but for spins measured at $f_{\text{ref}} = 20$ Hz. While the $\Delta\phi$ constraints are consistent between $f_{\text{ref}} = 20$ Hz and $t_{\text{ref}}/M = -100$, ϕ_1 is much better constrained at $t_{\text{ref}}/M = -100$.

Using the spins measured at $f_{\text{ref}} = 20$ Hz to generate the kick population results in distributions very similar to Fig. 3 of the main text. Once again, this is explained by the fact that the ϕ_1 and $\Delta\phi$ distributions at both $t_{\text{ref}}/M = -100$ and $f_{\text{ref}} = 20$ Hz are still consistent with a uniform

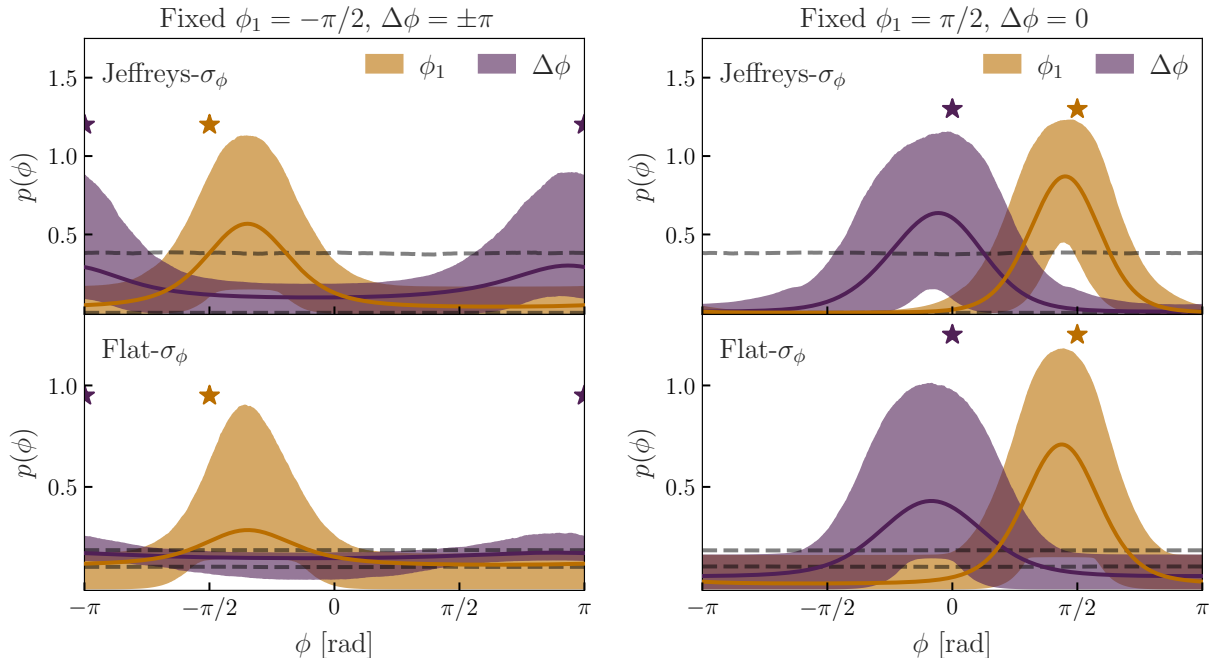


Figure S4. Same as Fig. 2, but for the two mock populations (with 31 events) described in Sec. II C. The left panels correspond to injections with fixed $\phi_1 = -\pi/2$ and $\Delta\phi = \pm\pi$ at $t_{\text{ref}}/M = -100$, while the right panels have fixed $\phi_1 = \pi/2$ and $\Delta\phi = 0$. The injected values are indicated by star markers. For both mock populations, the true values are reasonably well recovered, but the $\Delta\phi = 0$ population is better constrained than the $\Delta\phi = \pm\pi$ one, especially for the **Flat- σ_ϕ** prior.

distribution at 90% credibility, at current sensitivity.

To project measurements of the kick population with improved detector sensitivity, it is important to first appreciate that kick measurements for individual events do not depend on the reference point when using the method in Ref. [21]. The kick model **NRSur7dq4Remnant** [37] takes spins at $t_{\text{ref}}/M = -100$ as input; therefore, if spin measurements are available at $f_{\text{ref}} = 20$ Hz, they are first evolved using the **NRSur7dq4** dynamics from $f_{\text{ref}} = 20$ Hz to $t_{\text{ref}}/M = -100$ before computing the kick [37, 45]. As discussed in our companion paper [30], this is equivalent to measuring the spins directly at $t_{\text{ref}}/M = -100$. Therefore, by construction, we get the same kick velocity for individual events, independent of the reference point (modulo **NRSur7dq4** spin evolution errors, which are small compared to the model errors [37, 66]).

However, the same logic does not apply at the population level. Because the orbital-plane spin angles are poorly constrained at $f_{\text{ref}} = 20$ Hz for individual events, this information can get diluted at the population level (cf. Fig. S3). Therefore, even if we use the spin population at $f_{\text{ref}} = 20$ Hz and evolve spins drawn from this population to $t_{\text{ref}}/M = -100$, the orbital-plane spin angle information is already lost. On the other hand, at $t_{\text{ref}}/M = -100$, the orbital-plane spin angles are better constrained for both individual events [30] and on the population level (cf. Fig. S3), and this information can lead to improved kick population constraints. For this reason, we expect that as more observations become avail-

able, the ϕ_1 and $\Delta\phi$ populations will be significantly better constrained at $t_{\text{ref}}/M = -100$, leading to better kick population constraints as well.

C. Mock population study

To test the fidelity of the von Mises model in recovering ϕ_1 and $\Delta\phi$ populations, we conduct a mock population study. For each of our 31 events, we pick the maximum-likelihood posterior sample, but we rotate the orbital-plane spin angles and set them to constant values at $t_{\text{ref}}/M = -100$ for all events. We construct two such populations, one with $\phi_1 = -\pi/2$ and $\Delta\phi = \pm\pi$ and another with $\phi_1 = \pi/2$ and $\Delta\phi = 0$. We inject the corresponding signals in simulated detector noise and recover the spin population using our hierarchical analysis.

We use the **NRSur7dq4** waveform model for the injections as well as the parameter inference (with the **LAL-INFERENCE** package [62]). The signals are injected into Gaussian noise from a simulated LIGO-Virgo network at design sensitivity; however, we rescale the injected distance such that the SNR matches that of the observed event. Therefore, our mock populations approximately mimic the parameters and detector sensitivity for these events.

Figure S4 shows the results from our hierarchical analysis on these mock populations. For both mock populations, the ϕ_1 and $\Delta\phi$ distributions show a clear preference for

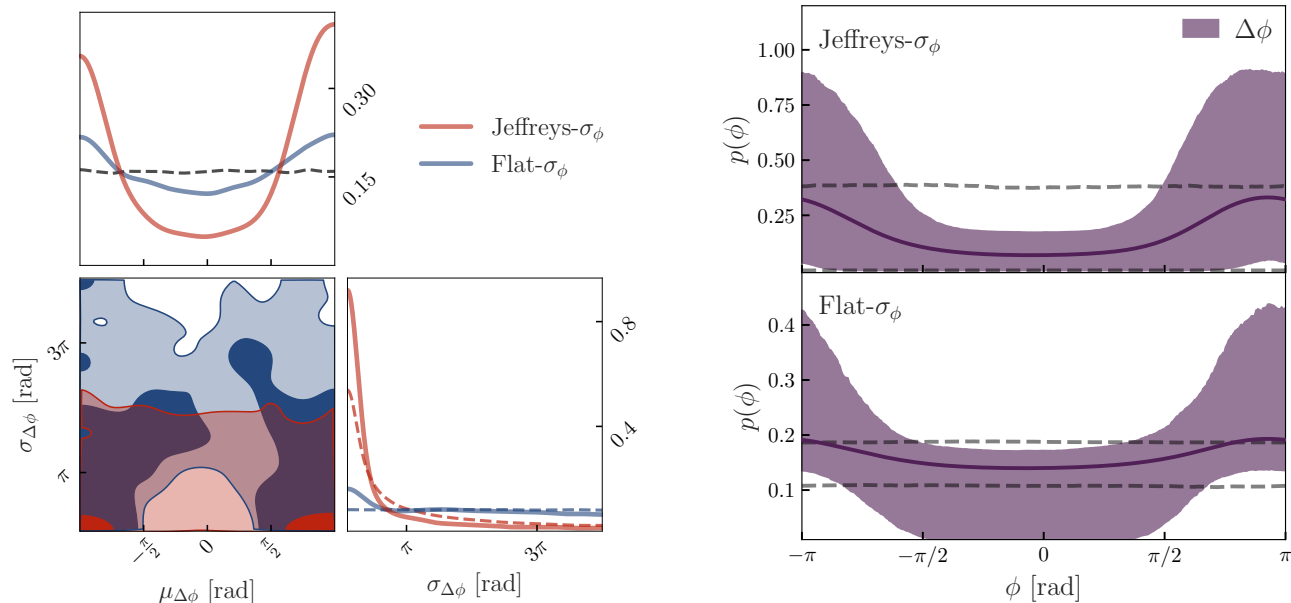


Figure S5. Constraints on the $\Delta\phi$ population at $f_{\text{ref}}=20$ Hz using all 46 binary BH events from GWTC-2. We use the `NRSur7dq4` model for the 31 events with $M \gtrsim 60M_\odot$, and the `IMRPhenomTPHM` model for the remaining 15 events. *Left*: Posteriors for the mean and width parameters for $\Delta\phi$. The shaded regions show 50% (dark shade) and 90% (light shade) credible bounds on the joint 2D posterior. The top and right subplots show 1D marginalized posteriors as solid lines. The prior on $\mu_{\Delta\phi}$ is shown as a dashed black line, while the two prior choices for $\sigma_{\Delta\phi}$ are shown as colored dashed lines. Unlike Fig. 2, we now see some information gain in the 1D posteriors for the width parameters, with a preference towards small widths. *Right*: Corresponding constraints on the $p(\Delta\phi)$ population distribution. The peak at $\Delta\phi \sim \pm\pi$ is amplified compared to Fig. 2.

the region near the injected values. In some cases, the peak locations are slightly offset from the injected values. Such shifts away from the true value are consistent with statistical error due to Gaussian noise. Interestingly, the $\Delta\phi = 0$ population is better recovered than the $\Delta\phi = \pm\pi$ population. This suggests that it is easier to constrain $\Delta\phi$ for binaries with $\Delta\phi = 0$, in agreement with Refs. [6, 7].

D. Results using all 46 GWTC-2 events

All results shown so far were restricted to the 31 signals with $M \gtrsim 60M_\odot$ so that we can use the `NRSur7dq4` model. In addition to generating `NRSur7dq4` posteriors for these 31 events, Ref. [30] also used the `IMRPhenomTPHM` [44] waveform model to analyze all 46 GWTC-2 binary BH events at $f_{\text{ref}} = 20$ Hz. We now repeat our analysis for all 46 binary BH events from GWTC-2, using the `IMRPhenomTPHM` posteriors from Ref. [30] for the remaining 15 events (listed in Tab. II of Ref. [30]). We use spins at $f_{\text{ref}} = 20$ Hz for all events, as spins at $t_{\text{ref}}/M = -100$ are

not available for `IMRPhenomTPHM`. Figure S5 shows constraints on the $\Delta\phi$ population using all 46 events. While we simultaneously model all spin degrees of freedom, we only show the $\Delta\phi$ population for simplicity. Similar to Sec. II B, the ϕ_1 population is not well constrained when the spins are measured at $f_{\text{ref}} = 20$ Hz.

The left-panel of Fig. S5 shows the posteriors for the $\mu_{\Delta\phi}$ and $\sigma_{\Delta\phi}$ parameters. Compared to Fig. 2, we now see that the 1D $\sigma_{\Delta\phi}$ posterior is distinguishable from the prior for both prior choices. In particular, there is a preference for small widths, while the $\mu_{\Delta\phi}$ distribution still peaks at $\sim \pm\pi$. As shown in the right-panel of Fig. S5, this leads to a stronger peak near $\sim \pm\pi$ in the $\Delta\phi$ population, compared to Fig. 2.

While this reinforces our results using only `NRSur7dq4`, it is important to consider that `IMRPhenomTPHM` can have biases in recovering the orbital-plane spin angles [30]. In addition, Ref. [30] found significant differences between the $\Delta\phi$ posteriors for `NRSur7dq4` and `IMRPhenomTPHM` for GW190521 [61]. This suggests that a detailed study of the impact of waveform systematics on the $\Delta\phi$ population is necessary. We leave this exploration to future work.